ESO “Advanced Study for Upgrades of the Atacama Large Millimeter/submillimeter Array (ALMA)”
(CFP/ESO/16/11115/OSZ)

High-cadence Imaging of the Sun

Final study report review data package - DS4

The potential of a high-cadence imaging mode for ALMA observations of the Sun

REVISED VERSION
July 31, 2023

(Original version: January 30, 2023)

Prepared by	Sven Wedemeyer Mikołaj Szydlarski	University of Oslo, Norway (UiO)
	M. Carmen Toribio Tobia D. Carozzi	Nordic ARC Node, Onsala Space Observatory (OSO), Sweden
Validated by		
Approved by		

Acknowledgements This work is supported by the SolarALMA project, which has received funding from the European Research Council (ERC) under the European Union’s Horizon 2020 research and innovation programme (grant agreement No. 682462, until September 2021), and by the Research Council of Norway through its Centres of Excellence scheme, project number 262622. The study team acknowledges support from the Nordic ALMA Regional Centre (ARC) node based at Onsala Space Observatory. The Nordic ARC node is funded through Swedish Research Council grant No 2017-00648.

Contents

1 Introduction 5

1.1 Context and background 5

1.2 Scope and aims of this report 6

2 Methodology 7

2.1 Outline 7

2.2 Software 8

2.3 Reference model 9

2.4 Uncorrupted measurement sets 9

2.5 Weather scenarios and corrupted measurement sets 10

2.6 Imaging 11

2.6.1 Basic imaging 11

2.6.2 Advanced imaging 12

3 Results 19

3.1 Basic imaging 19

3.2 Sliding time windows **20**

3.3 Self-calibration **20**

3.4 Self-calibration plus sliding time window **21**

3.5 Comparison of the different approaches **21**

4 Concluding remarks 33

1. Introduction

1.1 Context and background

The continuum radiation of the Sun emerges from its chromosphere — an atmospheric layer sandwiched between the photosphere and the corona. Despite its fundamental importance for the energy transport in the solar atmosphere, observations of the chromosphere are hampered by the small number of available diagnostics and the difficulties with interpreting them. The radiation continuum at millimeter wavelengths offers diagnostic possibilities for the study of our Sun that are complementary to commonly used diagnostics but which only now can be exploited thanks to ALMA's high spatial and temporal resolution. In particular, ALMA's ability to serve as an essentially linear thermometer of the atmospheric gas at unprecedented spatial and temporal resolution in the millimeter wavelength range has great scientific potential. Consequently, solar ALMA observations will contribute significantly to answering long-standing questions about the structure, dynamics and energy balance of the outer layers of the solar atmosphere and thus promise high-impact results (see Wedemeyer et al. 2016; Bastian et al. 2018, and references therein).

In contrast to many other astronomical sources, the Sun does fill and actually exceeds the primary beam of ALMA with a complex emission pattern that covers a large range of spatial scales *and* evolves on extremely short time scales of only seconds and even below. Consequently, the majority of solar science cases require imaging at high cadence, i.e. essentially snapshot imaging, which limits the visibility data available for imaging at any given time. Exploiting the time domain to its full extent within the instrumental limitations is therefore crucial for reliable imaging of solar ALMA data. The currently offered cadence of 1 s is already remarkable but an even higher cadence is technically possible.

The challenges with processing solar ALMA data during the past years have revealed the need for a thorough and systematic review and the further development of the current solar observing mode and the processing procedures of the resulting data, which differ significantly from the standard processing of other ALMA data. Please see Shimojo et al. (2017) and White et al. (2017) for a technical introduction to solar observing with ALMA. The experimental study presented here explores the potential of increasing the cadence of solar observing even further towards sub-second time resolution in order to increase the reliability of the resulting image time series.

Similar strategies that exploit a ultra-high cadence are already routinely applied for a long time for observations of the Sun at visible wavelengths. There, it is common to take rapid bursts of 50-100 images with high cadence and exposures of less than 100 ms. Each burst is then combined into one science-ready image by using MOMFBD (Multi-Object Multi-Field Blind Deconvolution, van Noort et al. 2005) or Speckle techniques (Labeyrie 1970; Wöger et al. 2008; Puschmann & Beck 2011). The advantage is that the atmosphere of the Earth above the telescope at the time of the observation does not vary notably during such a short exposure. This way the influence of the varying atmosphere above the telescope can (at least partially) be corrected for and leads usually to a substantial increase in image quality. ALMA observations are affected in a similar way, most notably in the form of phase corruptions caused in the Earth's troposphere. Further exploiting ALMA's high cadence for a possible reduction and correction of such phase errors is therefore promising. It should be mentioned that ultra-high time resolution imaging (at 20 ms) is already routinely performed at the Very Large Array (VLA), demonstrating that a similar capability would be worth introducing for ALMA, too.

1.2 Scope and aims of this report

This report aims at demonstrating the potential of exploiting a higher cadence of solar observing with ALMA for the future improvement and extension of the solar observing mode and more reliable imaging products. In particular, the aim is to investigate if combining visibility data from ultra-high cadence observations across sufficiently short time windows can increase the precision with which brightness temperature[1] maps can be reconstructed in the imaging process. Based on these experiments, first recommendations for potential future development steps are given.

[1]Please note that only interferometric observations are simulated for this report. No Total Power (TP) offsets are considered. The term brightness temperature is in this study used synonymously to the true brightness temperature minus a TP offset.

2. Methodology

2.1 Outline

In order to get a first idea about the potential prospects of exploiting a higher cadence for increasing the data quality for solar observations with ALMA, a small set of experiments has been carried out. For this purpose, we use sequences of artificial observations with a cadence of 100 ms (thus 600 frames for the covered 60 s) and apply phase corruption with the Solar ALMA Simulator (SASIM) for different weather scenarios (see Sect. 2.5). Here we restrict the analysis to the moderate and extreme scenarios as those are representative of situations for which advanced data processing may significantly improve the data quality. Measurement sets are produced with SASIM) for Band 3 and 6 for the uncorrupted case and for the selected scenarios. Standard data reduction and imaging is carried out for all frames of these measurement sets with the Solar ALMA Pipeline (SOAP), resulting in time series of images (in FITS format) at a cadence of 100 ms. These data correspond to those at 1 s cadence as described in the *Imaging Report* (Wedemeyer et al. 2023).

The two approaches for exploiting observations at higher cadence are illustrated in Fig. 2.1 and described below. In addition, self-calibration is considered.

Sliding time window.

A new processing mode of SOAP combines the visibility data across a user-specified time window that combines the data from neighbouring time steps (at 100 ms cadence) for producing one combined image each. As the central time step is increasing, the original cadence of 100 ms can be preserved.

Time-binning.

The sliding time results in an overlap of the time ranges that are used to construct the final images while maintaining the cadence of the input data. An alternative approach that avoids such overlap is to only construct images for consecutive time windows. While this time-binning approach will save computation time, the cadence of the final image series will be reduced to the user-selected time

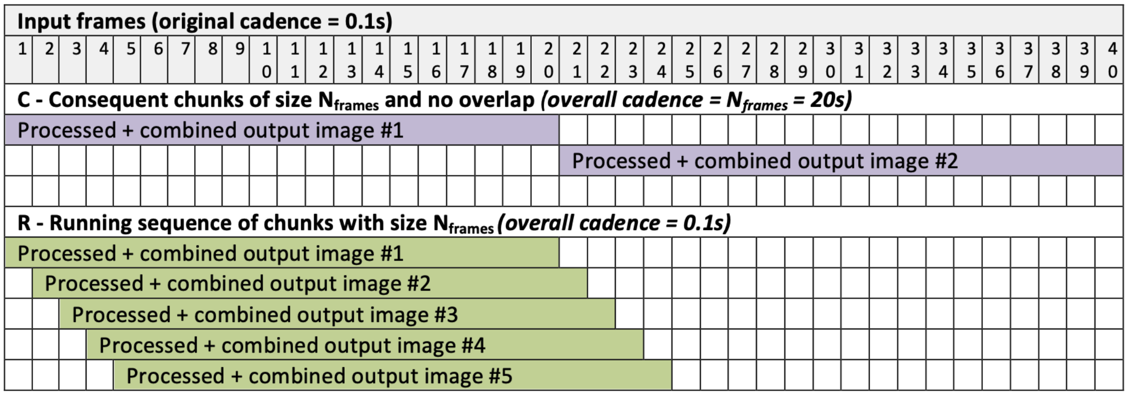

Figure 2.1: Illustration of the time-binning (top) and sliding time window (bottom) techniques for an example of 20 consecutive time steps at 0.1 s cadence.

window size. This mode has originally been referred to as "burst mode" in analogy to the observing techniques used for solar observations at visible wavelengths. During the development of the sliding time window technique, it became obvious that it also covers the planned burst mode. The latter would produce combined frames that are a subset of the sequences produced with the sliding time window technique. The burst mode is therefore no longer pursued separately as it is covered by the sliding time window mode.

Self-calibration

In general, self-calibration algorithms estimate and correct for the errors in the complex visibility measurements including those that are introduced by the instrumentation. It involves measuring the instrument's response to known signals, and then using that information to correct for errors in the measured data. This is typically done by applying a mathematical model that describes the instrument's response and the errors it introduces. It should be noted that, for radio/(sub)-mm interferometric observations, self-calibration can be applied on phases and amplitudes and that sufficient information on the source model is required, which will be complex for a time varying source like the Sun.

The estimate of the errors can be done by minimizing the difference between the observed and modeled visibilities. Once the errors are estimated, the visibility measurements are corrected by dividing the observed visibilities by the estimated errors. The corrected data is then used to reconstruct the final image. Self-calibration usually results in more accurate imaging. For solar observations, however, the pronounced time variability of the source poses particular challenges. While an adequately long time window is needed to ensure the construction of a accurate sky model, temporal variations of the source can make this fundamental part of the self-calibration process difficult.

2.2 Software

The following software packages and codes are used for this study:

- The stellar atmosphere simulation code **Bifrost** (Gudiksen et al. 2011) is used for the production of time sequences of 3D solar model atmospheres.

- The **Advanced Radiative Transfer (ART) code** (De La Cruz Rodríguez et al. 2021) calculates synthetic brightness temperature maps that are used as input for SASIM.
- The **Solar ALMA Simulator (SASIM)** is the main software package developed for this study. SASIM takes time series of synthetic brightness temperature maps as input and applies instrumental and weather (or "seeing") effects. The output is a simulated measurement set.
- The **Solar ALMA Pipeline (SOAP)** is the main tool used for the reconstruction of time series of brightness temperature maps. SOAP accepts as input measurement sets as downloaded from the ALMA Science Archive but also simulated measurement sets produced with SASIM.

Please see the related reports *Imaging Report* (Wedemeyer et al. 2023) and *Tech. Doc.* (Wedemeyer et al. 2023) and also Wedemeyer et al. (2022) for further information.

2.3 Reference model

As for the 1 s cadence series, the original ART maps at 0.1 s cadence, i.e. the data used as input for constructing the uncorrupted measurement sets with SASIM, are averaged over frequency and then convolved with a synthesised beam. This results in 600 reference maps covering a duration of 60 s at 0.1 s s cadence. The same synthesised beams as for all SOAP calculations used in this part of the study is chosen. The chosen beams for the parameter `robust=0.5` (see Sect. 2.6) have the following properties:

	Major axis [arcsec]	Minor axis [arcsec]	Angle [degree]
Band 3	1.865	1.334	80.99
Band 6	0.805	0.571	81.63

Accordingly, a reference model is derived for each receiver band each time frame. The resulting reference maps for Band 3 and Band 6 for the first time step in the series are shown in Fig. 2.3a-b.

2.4 Uncorrupted measurement sets

Following the approach described in detail for the imaging parameter study by *Imaging Report* (Wedemeyer et al. 2023), realistic sky models are constructed based on state-of-the-art 3D time-dependent radiation magnetohydrodynamic simulations as produced with the BIFROST code (see Sect. 2.2). For this study, a sequence with a duration of 60 s at 0.1 s cadence (i.e. 600 time steps) is used. Each of these 600 3D models is then used as input for the Advanced Radiative Transfer (ART) code that produces intensity maps at frequencies corresponding to ALMA's receiver bands 3 and 6 as offered for solar observations. These time series of maps are converted into flux and then used as input for the Solar ALMA Simulator (SASIM), which generates corresponding measurement sets.

The result is a (uncorrupted) measurement set for a solar science target for each Band 3 and 6. In addition, corresponding measurement sets for a calibrator source are produced for both bands. As detailed in the *Imaging Report* (Wedemeyer et al. 2023), the calibrator maps have a central pixel with

Parameter	Description	Default
`pwv`	Total precipitable water vapour in mm	3.0
`deltapwv`	RMS PWV fluctuations *as a fraction of PWV parameter*	0.15
`beta`	Exponent of fractional brownian motion	1.1
`windspeed`	wind speed for screen type corruption (m/s)	7.0
`noiselevel`	additional phase noise as set in the simplenoise mode of setnoise.	0.0

Table 2.1: Controllable parameters for the phase corruption with SASIM. Please note that this parameters are passed on to the CASA functions ***settrop*** and ***setnoise***.

a constant flux of 7 Jy and all other pixels are set to zero. These maps are processed with SASIM in same way as for the science target. Apart from the higher cadence, the same simulation setup as for the 1 s case as described in the *Imaging Report* (Wedemeyer et al. 2023) is used, i.e. observations around local noon in array configuration 3 with baselines up to 500 m.

Please see Fig. 2.3c-d for examples of images as produced with SOAP parameters with standard imaging parameters (as described in Sect. 2.6) from the uncorrupted MSs.

2.5 Weather scenarios and corrupted measurement sets

The uncorrupted measurement sets (see Sect. 2.4) can be further processed with SASIM in order to simulate the impact of Earth's atmosphere (and instrumental effects) on the measured visibilities. The resulting phase corruption is controlled with the parameters shown in Table 2.1. Please note that the additional parameter `simint = 0.1` has to be set for the processing of the time series used here[1]. As described in the *Imaging Report* (Wedemeyer et al. 2023), the parameter `pwv` for the perceptible water vapour (PWV) level alone does not produce measurement sets that are representative of real daytime solar observing conditions, even when matching the PWV that is reported for such observations. Instead realistic SASIM parameters are determined by matching the median and variation of the Spatial Structure Function (SSF) of the resulting simulated calibrator measurement set (as part of large parameter grids) to the SSFs of selected observational ALMA calibration measurement sets. This approach was applied to a number of representative observing conditions, here also referred to as weather scenarios, for the optimisation of the imaging procedure at 1 s cadence as detailed in the *Imaging Report* (Wedemeyer et al. 2023). While these scenarios were developed based on 1 s cadence data, both for the simulated and most of the real measurement sets, they are applicable to the data at 0.1 s cadence, too.

For exploring the potential of solar observing at higher cadence as described in this report, the scenarios *moderate* and *extreme* are selected. The corresponding SASIM parameters are provided in Table 2.2. The resulting phases of the corrupted calibration measurement sets are illustrated in Figs. 2.4-2.7 for selected baselines. For comparison, the corresponding results for the measurement sets at 1 s cadence are plotted, too. Clearly, the phase variations are already significant for the moderate scenario and even much more pronounced for the extreme scenario, thus posing challenges

[1] D. Petry (ESO) kindly provided an updated version of CASA that allows to set shorter time steps for settrop() via the new additional parameter. Please see the *Tech. Doc.* (Wedemeyer et al. 2023) for details.

		SASim parameters					Corrupted MS	
#	Description	PWVa	dPWV	beta	wspd	smpn	SSF-M	SSF-V
Band 3								
4	Moderate	2.20	0.45	1.10	7.00	0.80	8.17	1.02
7	Extreme	8.00	0.45	1.10	20.00	2.00	29.91	3.06
Band 6								
4	Moderate	2.00	0.03	1.10	1.00	1.40	8.18	1.18
7	Extreme	8.00	0.03	1.10	20.00	2.00	30.70	3.15

Table 2.2: Selected scenarios for Band 3 and Band 6 as defined by the median and variation of the Spatial Structure Function (SSF) based on measurement sets obtained with ALMA. Each scenario is matched with a simulated measurement set that produces a SSF with similar median and variation values. The corresponding SASim corruption parameters are listed for each scenario.

for the imaging step as intended. This effect can also be seen in the SSF plots in Fig. 2.2 and the resulting values for the median (SSF-M) and variation (SSF-V) of the SSFs. Please note that the XX and YY phases cover the same value ranges in the SSF plots so that mostly the YY data is visible.

2.6 Imaging

2.6.1 Basic imaging

Imaging is performed for the uncorrupted and corrupted science target measurement sets for each frame independently. Applying SoAP (see Sect. 2.2) then results in time series of 600 frames for each measurement set. The resulting data is illustrated in Fig. 2.3. The following default SoAP (CLEAN) parameters were used:

```
niter: 1000
robust: 0.5
gain: 0.025
cycleniter: -1
```

Please note that neither the brightness temperature maps for the spectral channels nor the reference model maps are multiplied by the primary beam prior to being used as input for SASim. Application of the primary beam occurs as part of ***simobserve()*** when it is called during the execution of SASim. Please note that a mask (based on the primary beam response) is applied within SoAP and also to the reference model maps. Please refer to the *Tech. Doc.* (Wedemeyer et al. 2023) for more information regarding SoAP and the parameters.

Already by comparing the maps for the same single time step in Fig. 2.3, the impact of the phase corruption becomes clearly visible. Stronger corruption as simulated in the extreme scenario indeed adds noise to the final maps as intended. These results and the corresponding results for the measurement sets for the original cadence of 1 s will be used as reference for the imaging strategies that exploit the time domain for improving the overall image quality.

	self-calibration	twsize [s]
X	—	—
W1	—	1.0
W2	—	2.0
W5	—	5.0
W10	—	10.0
S	yes	—
SW1	yes	1.0
SW2	yes	2.0
SW5	yes	5.0
SW10	yes	10.0

Table 2.3: Considered imaging cases.

2.6.2 Advanced imaging

The corrupted measurement sets for Band 3 and Band 6 are processed with SoAP with the following options:

- **Standard imaging:** SoAP is used with the default imaging parameters (see Sect. 2.6) without sliding time windows and without self-calibration.
- **Sliding Time Window:** This option is activated and controlled with the SASim-SoAP parameter `twsize` specified in units of seconds. Setting this parameter to `null` deactivates this option. This approach can be used with SoAP level as set with parameter `lvl`. The input measurement set can also be the result of a prior self-calibration step.
- **Self-calibration** of a measurement set with SoAP is carried out by setting the SASim-SoAP parameter `lvl` to 3. The procedure then starts with the window size as set with the parameter `max_window_size` and iterates until the window size set by the parameter `min_window_size` is reached. The results are then saved as a new measurement set. For this study, `max_window_size=30` and `min_window_size=1` are used, which results in six iterations with self-calibration windows of 30, 15, 8, 4, 2, and finally 1 s.

First, the corrupted measurement sets are processed with SoAP-level 2 without sliding time windows and then for a range of values for the sliding window size (`twsize`). Then, self-calibration is applied to the corrupted measurements sets. Finally, the resulting self-calibrated measurements sets are used for imaging with toolSoAP-level 2 for the same values of `twsize` as above. The considered cases are summarised in Table 2.3.

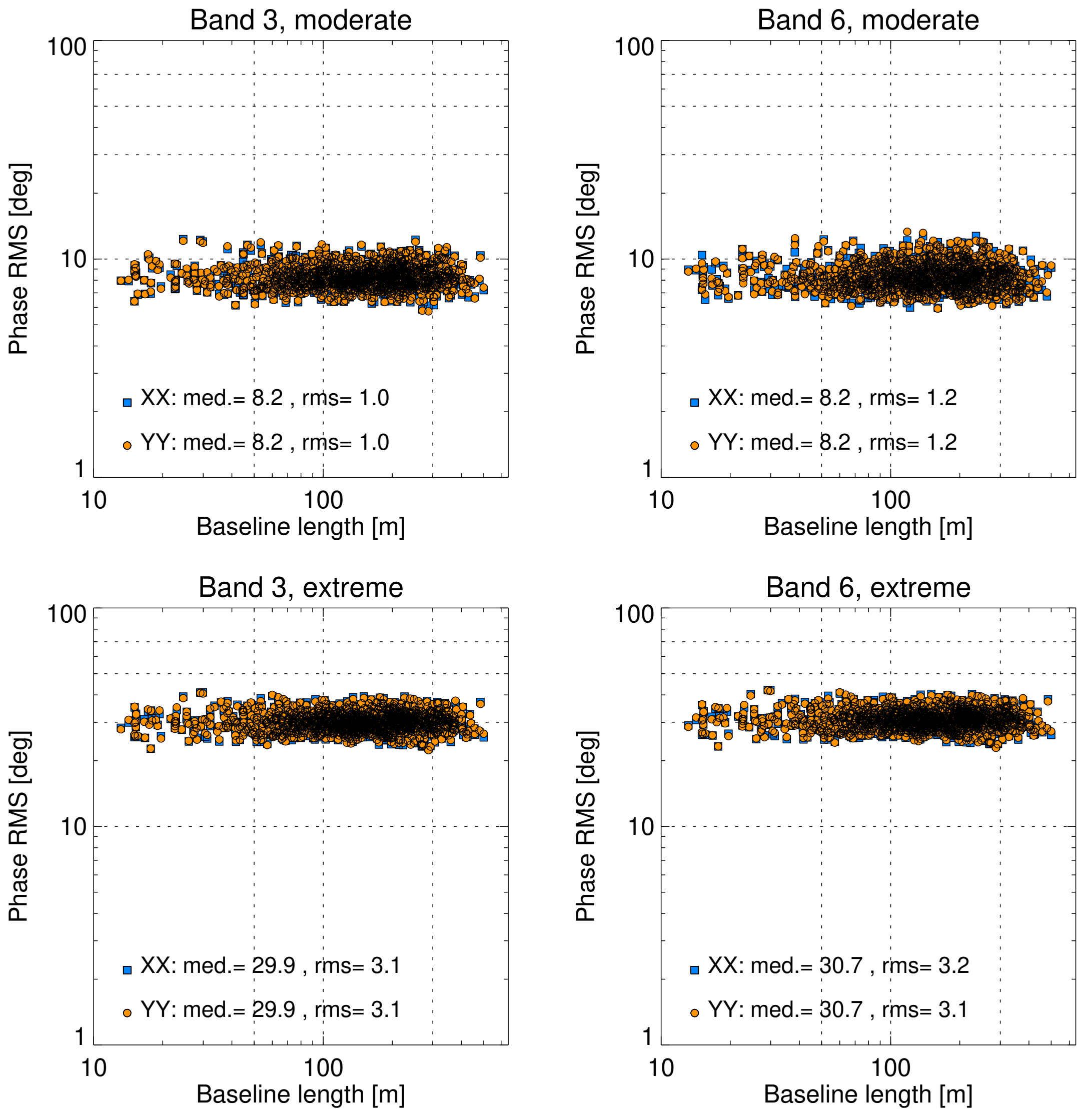

Figure 2.2: Spatial Structure Function (SSF) for Band 3 (left column) and Band 6 (right column) for the corrupted measurement sets for the scenarios moderate (top) and extreme (bottom).

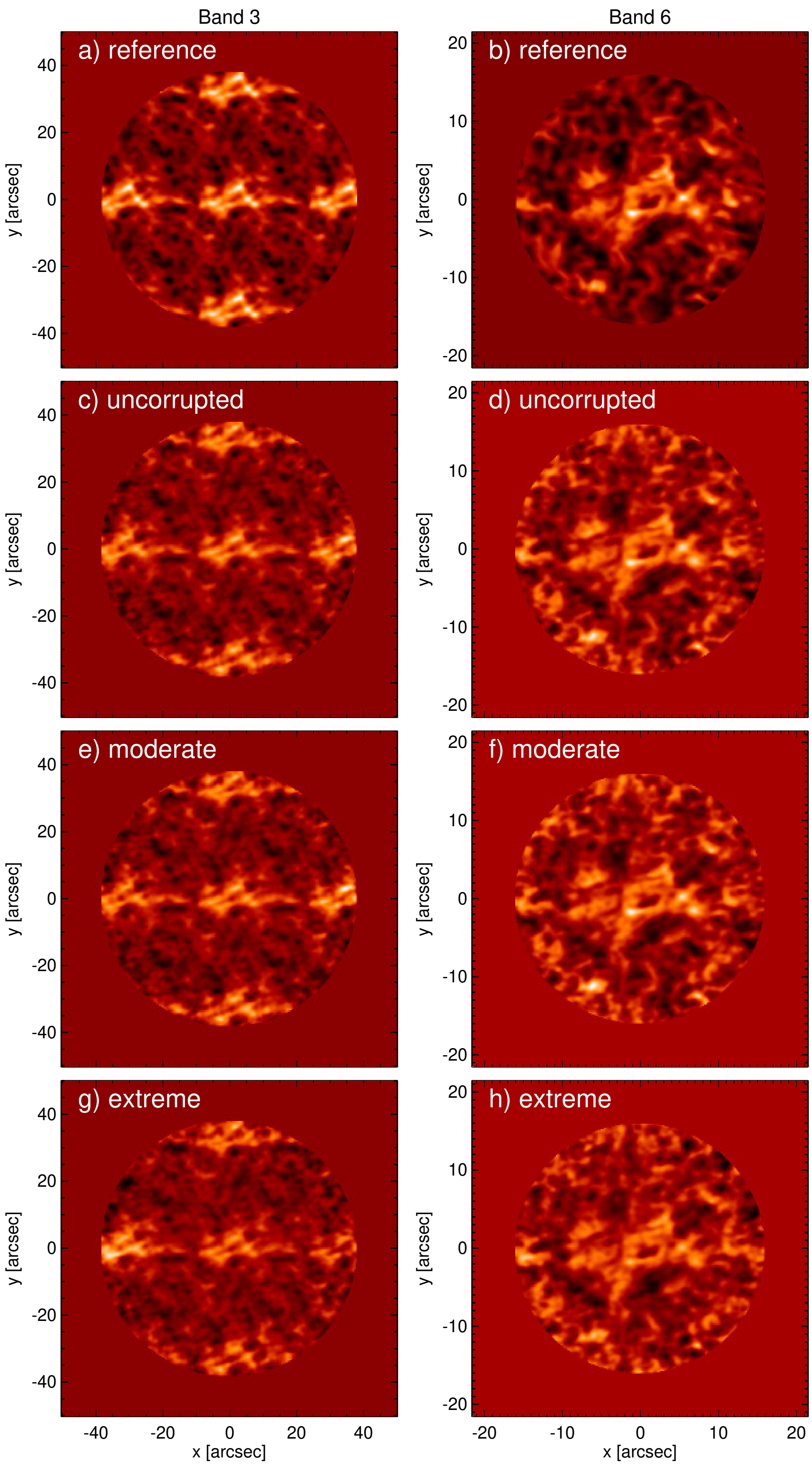

Figure 2.3: Brightness temperature maps for the first time step in the 0.1 s cadence series for Band 3 (left) and Band 6 (right). From top to bottom: The reference sky model (a-b), the imaging results for the uncorrupted case (c-d), and for the corrupted MS for the cases moderate (e-f) and extreme (g-h).

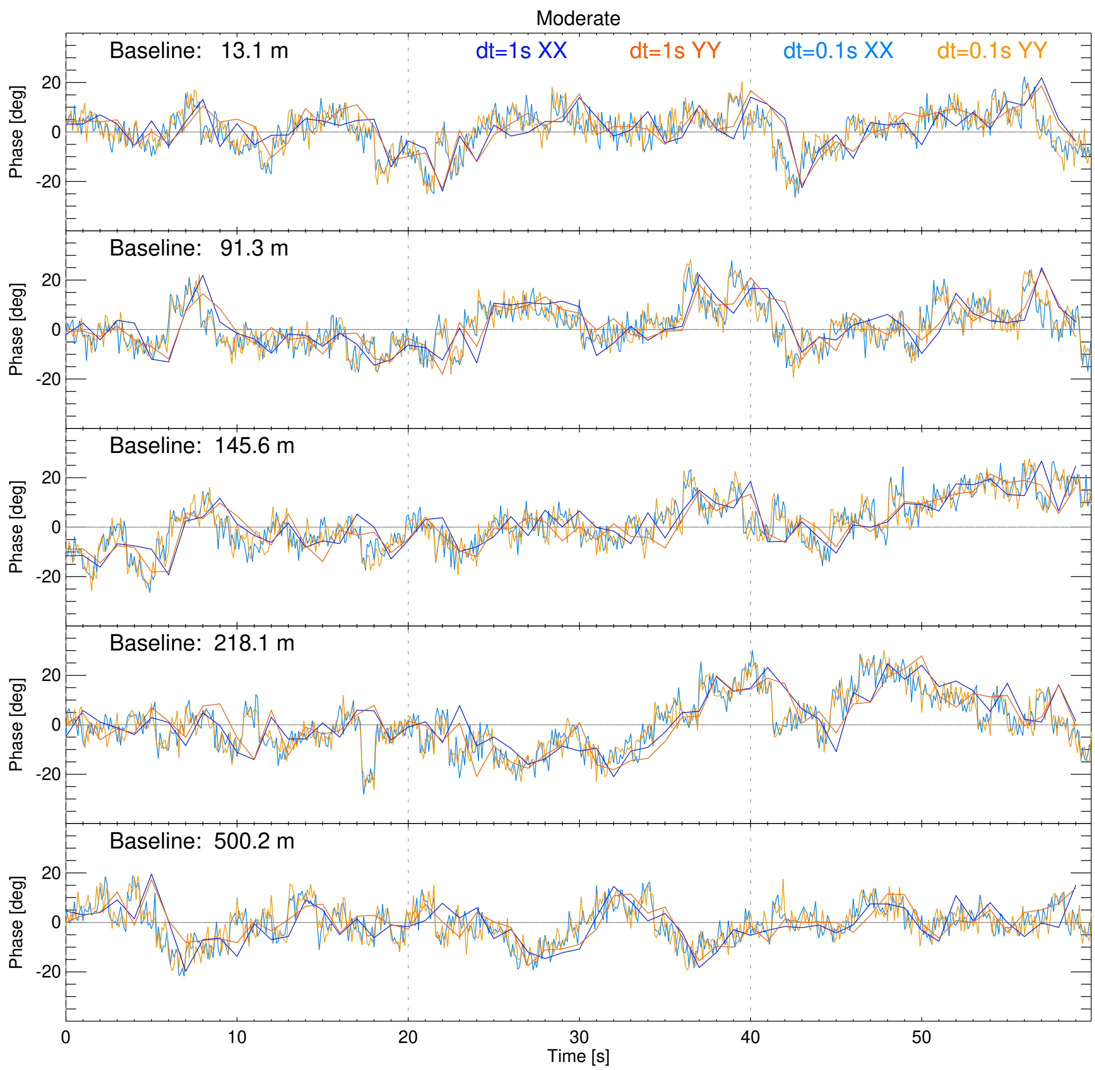

Figure 2.4: Phase as function of time for the Band 3 calibrator measurement set for the scenario moderate. The XX and YY phases for the corrupted measurement sets at a cadence of dt=0.1s (dark blue and orange lines) are compared to the corresponding simulations at 1.0 s cadence (light blue and dark yellow). A color legend is provided in the topmost panel.

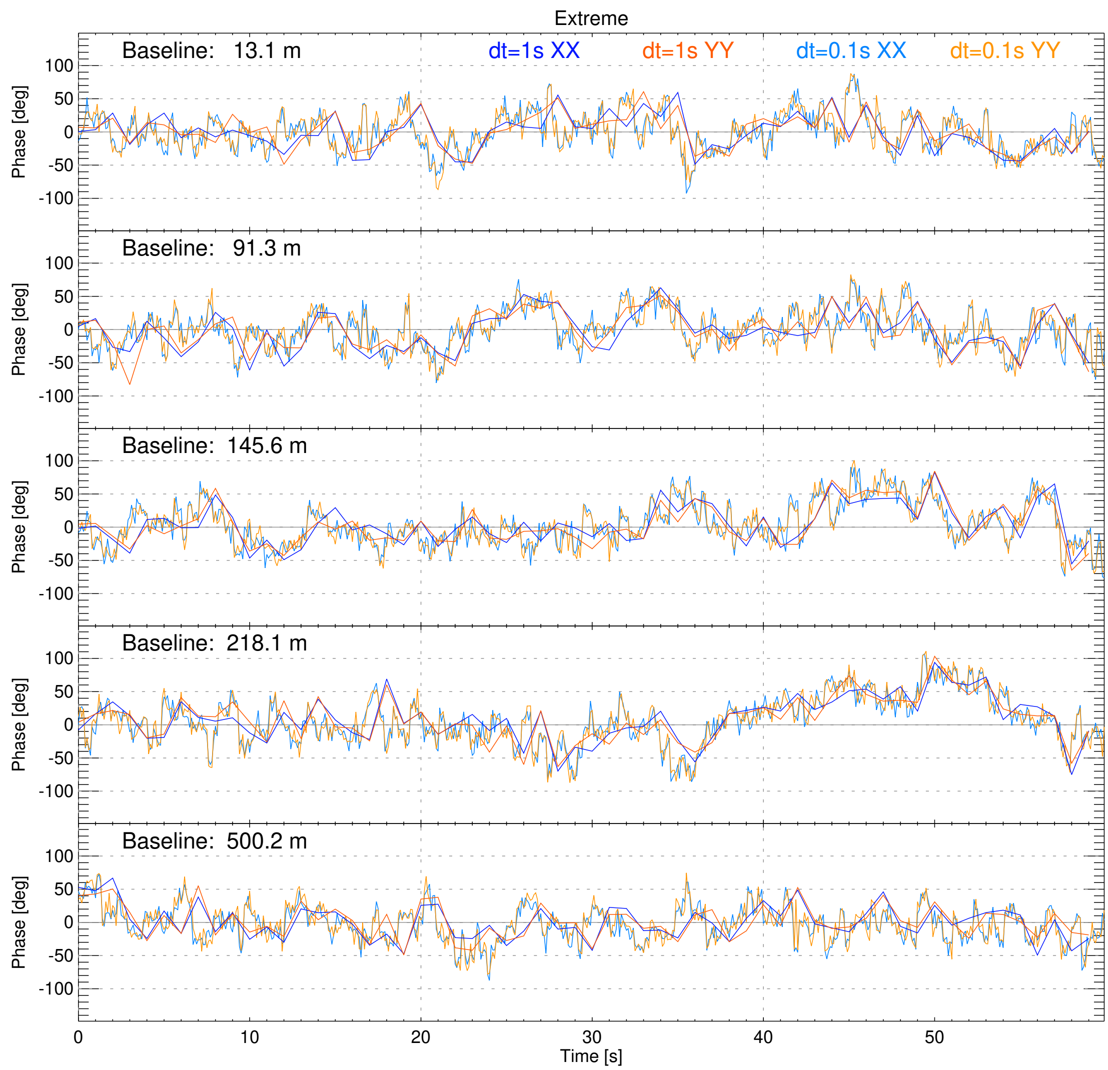

Figure 2.5: Phase as function of time for the Band 3 calibrator measurement set for the scenario extreme. The XX and YY phases for the corrupted measurement sets at a cadence of dt=0.1s (dark blue and orange lines) are compared to the corresponding simulations at 1.0 s cadence (light blue and dark yellow). A color legend is provided in the topmost panel.

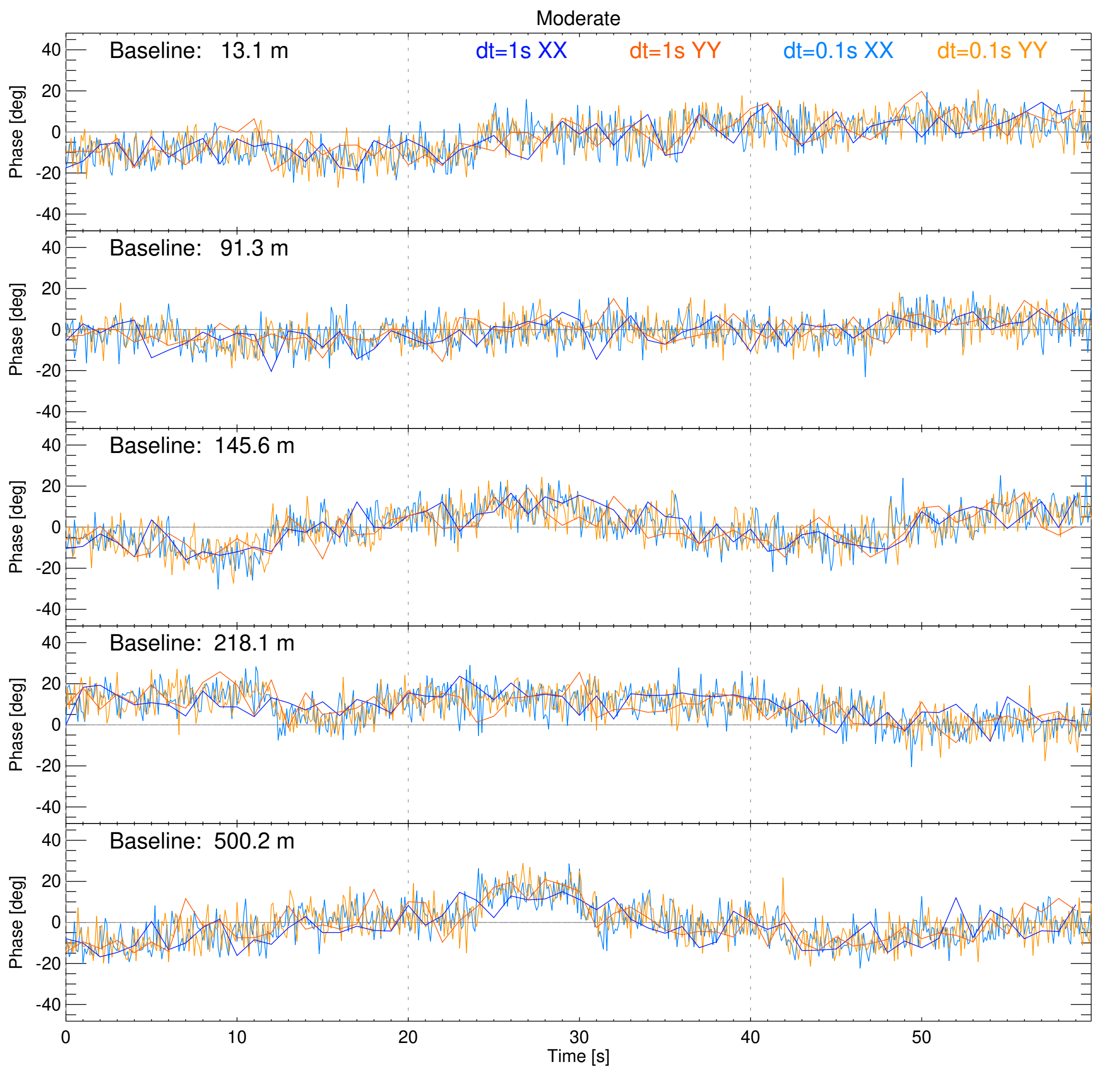

Figure 2.6: Phase as function of time for the Band 6 calibrator measurement set for the scenario moderate. The XX and YY phases for the corrupted measurement sets at a cadence of dt=0.1s (dark blue and orange lines) are compared to the corresponding simulations at 1.0 s cadence (light blue and dark yellow). A color legend is provided in the topmost panel.

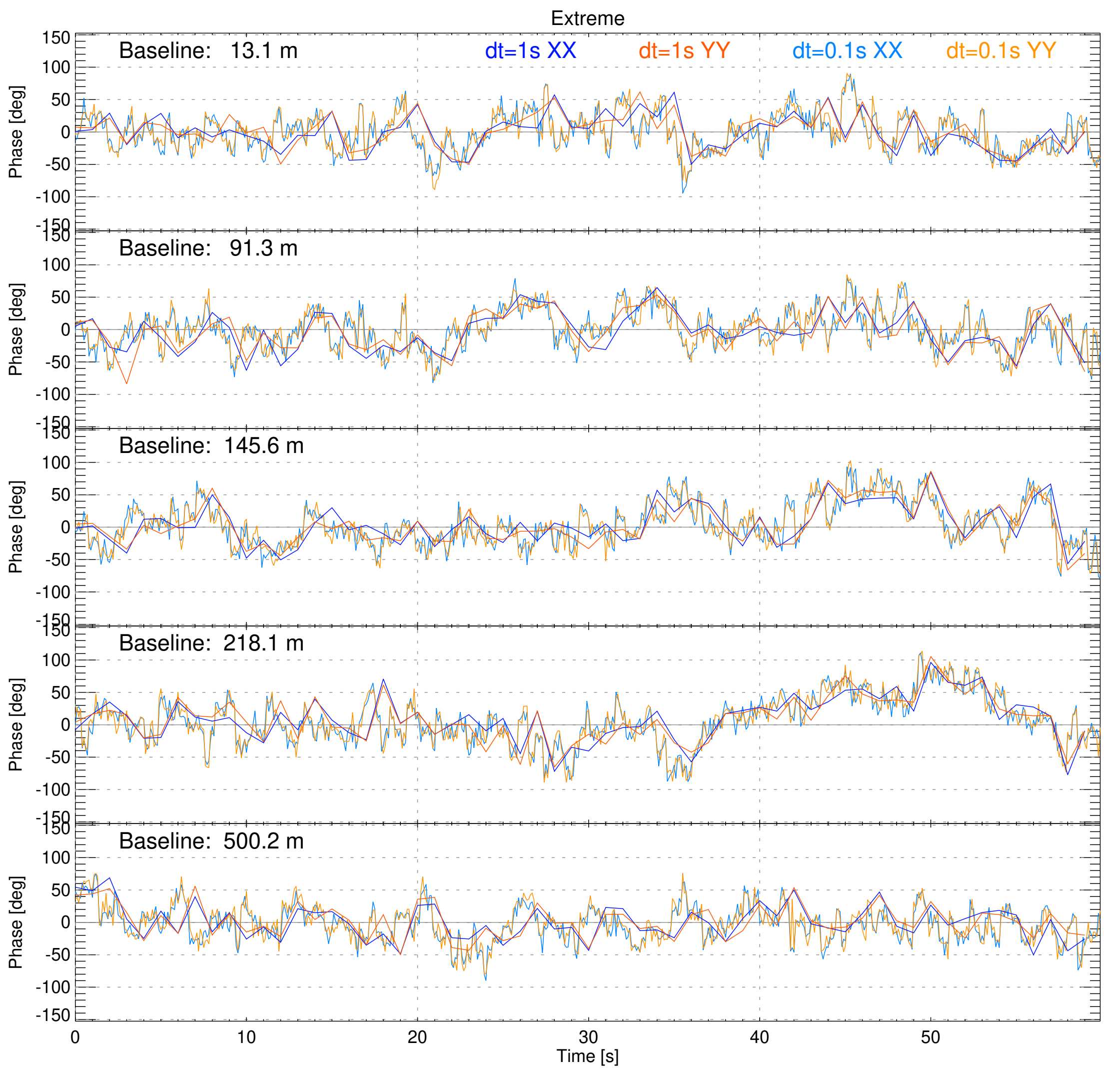

Figure 2.7: Phase as function of time for the Band 6 calibrator measurement set for the scenario extreme. The XX and YY phases for the corrupted measurement sets at a cadence of dt=0.1s (dark blue and orange lines) are compared to the corresponding simulations at 1.0 s cadence (light blue and dark yellow). A color legend is provided in the topmost panel.

3. Results

For comparison with the imaging runs with sliding time windows and/or self-calibration, first the results from the basic imaging runs are discussed in Sect. 3.1. The resulting changes of the brightness temperature time series are visualised in Figs. 3.1-3.4 for Band 3 and Band 6 for the moderate and extreme scenario. The results are compared to the (uncorrupted) reference case and the corresponding measurement sets for the original cadence of 1 s for a selected pixel position in the inner field-of-view (FOV) and for the brightness temperature averaged over the FOV. The results for the sliding time windows, for self-calibration, and a combination thereof are discussed in Sects. 3.2 -3.4, respectively, and then compared in Sect. 3.5.

3.1 Basic imaging

Both the results of standard imaging for the data at 1 s and at 0.1 s cadence show a noise component with fluctuations on the order of 100 K for the moderate scenario for Band 3 when considering individual positions in the FOV which strongly suppressed when averaging across the FOV (see Fig. 3.1). In addition, there is typically an offset of a few 100 K with respect to the reference model, which varies from position to position. An offset of $\sim$ 100 K still persists in the spatially averaged brightness. While no exact match with the reference model is expected given that the simulated observations have by nature a limited *uv*-coverage, this potentially systematic offset should be further investigated and taken into account for the future development of imaging algorithms for solar ALMA data. This effect is also visible in the moderate scenario for Band 6 although much less pronounced (see Fig.3.3). The deviation from the reference is even reduced to $\sim$ 10 K in the spatially averaged brightness temperature.

By design, the extreme scenario does exhibit a higher level of remaining variations and thus deviation from the reference model (see Figs. 3.2 and 3.4). For Band 3, again an offset with respect to the reference model remains in the spatially averaged brightness temperature, amounting to 50-100 K. For Band 6, the averaged brightness temperature fluctuates around the reference model with variations of only around a few 10 K.

3.2 Sliding time windows

The top four rows of Figs. 3.1-3.4 show the brightness temperature (red curves) that results from applying sliding time windows with widths from 1 s to 10 s for selected positions in the FOV and for the spatially averaged maps. The gain with a 1 s window applied to the 0.1 s-cadence data as compared to the unaltered 1 s-cadence data is notable but small for moderate scenario for Band 3 and even smaller for Band 6. This outcome is expected as basic imaging is already performing reasonably well under these conditions, maybe except for the systematic offset for Band 3. A longer time window does not result in any notable improvement for the tested Band 6 case but further suppresses the noise visible for Band 3 (Fig. 3.1).

The benefits of applying sliding time windows are clearly larger for the extreme scenario. Here, applying a 1 s window to the 0.1 s-cadence data already shows less noise as compared to the unaltered 1 s-cadence data (Figs. 3.2 and 3.4). Increasing the width of the time window then substantially reduces the noise and thus the deviation from the reference model for both considered receiver bands. The brightness temperatures deviations remain on a level of a few 100 K for individual pixels over time so that scientific studies need to consider this error when analysing such time series. On the positive side, however, measurement sets that are obtained under such extreme conditions still can produce scientifically valuable data with the help of sliding time windows.

3.3 Self-calibration

The corrupted measurement sets for the moderate and extreme scenario for Band 3 and 6 were processed with SoAP with self-calibration (SoAP level 3, see Sect. 2.6.2 and the *Tech. Doc.*, Wedemeyer et al. 2023). The resulting time variation of brightness temperatures calculated with self-calibration are shown in the middle row of Figs. 3.2 and 3.4. There is only little improvement for the Band 3 moderate scenario with remaining small fluctuations on the level of what is produced with basic imaging for the 1 s and 0.1 s cadence data. In contrast, there is a notable reduction in noise for the Band 3 extreme scenario, clearly demonstrating the advantage of applying self-calibration under such conditions and thus salving otherwise strongly affected measurement sets. However, a small but systematic offset with respect to the reference model remains. In the spatially averaged brightness temperature maps, the offset at the beginning of the time series is almost 150 K but decreases during the first 30 s and then levels off to a value of $\sim$ 70 K. As before, there is not much gain for the Band 6 moderate scenario as the noise level was low to start with. In contrast, the Band 6 extreme scenario immediately benefits from a strong reduction in noise and a very low offset in the spatially averaged brightness temperature maps. For individual pixels, however, offsets of a few 100 K with respect to the reference model must be expected. It is important to note that the deviations and thus the final systematic offsets are measured with respect to a reference model that in reality never can be matched by data obtained with an interferometric array with a finite number of baselines. The reference model corresponds to a single-dish telescope with the same angular resolution as the synthetised beam of the simulated array but with perfect *uv*-coverage and no atmospheric or instrumental degradation (see Sect. 2.6 in the *Tech. Doc.* (Wedemeyer et al. 2023)). We recommend therefore to review in a future study if more suitable reference models can be constructed and/or if an algorithm can be devised that corrects for the brightness temperature offsets that might likely be due to the nature of observing a complex source like the Sun with an interferometric array.

3.4 Self-calibration plus sliding time window

The self-calibrated measurement set produced with SOAP level 3 is now used as input for imaging with sliding time windows. The resulting time variation of brightness temperatures calculated with a combination of self-calibration and sliding time windows are shown in the lower four rows of Figs. 3.2 and 3.4. Applying a time window of 1 s width to the Band 3 moderate data has no obvious benefits and can lead even result in slightly higher deviations from the reference model as compared to the self-calibrated data without sliding time windows. Larger windows again smooth the variations but result in a slightly larger offset than the data without self-calibration. In conclusion, there seem not to be strong benefits of combining self-calibration and sliding time windows for the Band 3 moderate scenario. The same is true and even more obvious for the Band 6 moderate scenario, which also remains with a larger offset although only a ~ 20 K level. For the extreme scenario for Band 3, already a time window of 1-2 s produces notably smoother time series both for individual pixels and for the spatially averaged maps. The offset from the reference model is larger on average but comparable to the basic imaging results for some pixels. In contrast, there is no notable gain from combining self-calibration with sliding time windows for the extreme scenario for Band 3. Overall, additionally applying a time window with a width of 1-2 s can improve the results for self-calibrated data but the improvements remain moderate in comparison to data that has been treated with either only sliding time windows or only with self-calibration.

3.5 Comparison of the different approaches

The quality of the imaging results is now quantified with respect to the corresponding reference model (see Sect. 2.3). For each case shown in Table 2.3 and each considered band and scenario, the difference between the corresponding brightness temperature maps ($T_\mathrm{b}(x,y,t)$) and the reference map ($T_\mathrm{b,ref}(x,y,t)$) for all time steps is calculated:

$$\Delta T_\mathrm{b}(x,y,t) = T_\mathrm{b}(x,y,t) - T_\mathrm{b,ref}(x,y,t) \tag{3.1}$$

Only pixels within the circular mask are considered. Please see Fig. 3.5 for examples of the resulting difference maps as produced with basic imaging for both bands for the moderate and extreme scenario. The first time step of these time series is used for illustration. As expected, the moderate scenario for Band 3 shows the smallest brightness temperature differences and thus the smallest deviation from the reference case. In other words, the sky image of the solar target was reconstructed with reasonable accuracy. Except for a few positions the differences remain below 100 K in the inner part of the field-of-view (see red histogram in Fig. 3.5b) but increase to 200-300 K at the outer parts of the FOV. The other examples and all maps in general show a similar increase of the deviation with increasing distance from the centre of the FOV (i.e., the axis) as a result of the primary beam response and the resulting signal-to-noise ratio. The overall level of the brightness temperature differences, however, is notably higher for the moderate scenario for Band 6 as observations at the higher frequencies in this band are more severely impact by the tropospheric phase corruption as compared to Band 3. The deviations are typically on the order of up to a few 100 K for the extreme scenario and can even exceed 500 K in the outer parts of the FOV (see Fig. 3.5c-d).

Radial dependence

Due to the primary beam response and the resulting change of the signal-to-noise ratio, the deviation of the reconstructed brightness temperatures from the reference model changes with increasing radius outwards from the axis (centre of the FOV). This effect is clearly visible in the examples in Fig. 3.5 both in the maps and in the different histograms. The outer parts of the FOV clearly exhibits the highest deviations. In principle, the requirements of a given scientific application would determine if imaging with high accuracy is needed only for the innermost region of the FOV or rather for the whole FOV as considered here.

The radial dependence of the deviations from the reference model(s) is therefore visualised in more detail for all considered imaging cases in Fig. 3.6. In conclusion and as expected, the deviations are highest towards the edges of the considered FOV. On the other hand, the deviations remain at a smaller level for radii of $\sim 70\,\%$ of the FOV radius. It is also notable that the remaining offsets discussed in the previous sections are lower for the sliding time window map series as compared to the sets with self-calibration.

Brightness temperature differences

Histograms of all brightness temperature differences ΔT_b, i.e. the deviations from the corresponding reference model, are shown for all considered imaging cases in Fig. 3.7. It is most obvious that the imaging runs with self-calibration produce much broader distributions than the basic imaging results and the runs with sliding time windows but no self-calibration. Also, as concluded in the previous sections, there is no obvious benefit from combining self-calibration with additional sliding time windows, at least in most situations. On the other hand, the extreme scenarios for Band 3 and 6 demonstrate that sliding time windows can result in a significant noise reduction and might thus have potential of salvaging otherwise highly problematic measurement sets.

Final comparison

For each of the resulting data cubes of brightness temperature differences for the considered imaging cases, the average (TDM) and the standard variation (TDV) of the absolute differences are calculated:

$$\mathrm{TDM} = \langle |\Delta T_\mathrm{b}|(x,y,t) \rangle_{x,y,t} \tag{3.2}$$

$$\mathrm{TDV} = \frac{1}{N} \sqrt{\sum (|\Delta T_\mathrm{b}|(x,y,t))^2} \tag{3.3}$$

A pair of TDM and TDV values is therefore derived for each imaging case and each considered band and scenario. The results, which are illustrated in Fig. 3.8, confirm the conclusion of the previous sections that a sliding time window can reduce the deviations in extreme situations but that some offsets with respects to the reference models and thus the true sky model remain. Overall, the median brightness temperature error in the reconstructed brightness temperature and also the offset are typically on the order of 200 K for basic imaging and when applying sliding time windows but closer to 300 K when applying self-calibration.

However, brightness temperature differences as metric do not fully capture the internal consistency of the reconstructed time series. For that reason, the rate of change (RoC) was calculated for the same data, again restricting the analysis to the inner 70 % of the brightness temperature maps. The corresponding variance of the RoC provides a good metric for the relative fluctuations of a time series:

$$\mathrm{VRoC} = Var\left(\frac{|\Delta T_{\mathrm{b}}|(x,y,t_{i+1}) - |\Delta T_{\mathrm{b}}|(x,y,t_i)}{|\Delta T_{\mathrm{b}}|(x,y,t_i)}\right) \tag{3.4}$$

The results are shown in Fig. 3.9 for all considered imaging cases. This metric reveals the benefits of applying sliding time windows for noise reduction. The moderate scenario for Band 6 again sticks out as it is less severe than the other cases and does not benefit from any further noise reduction.

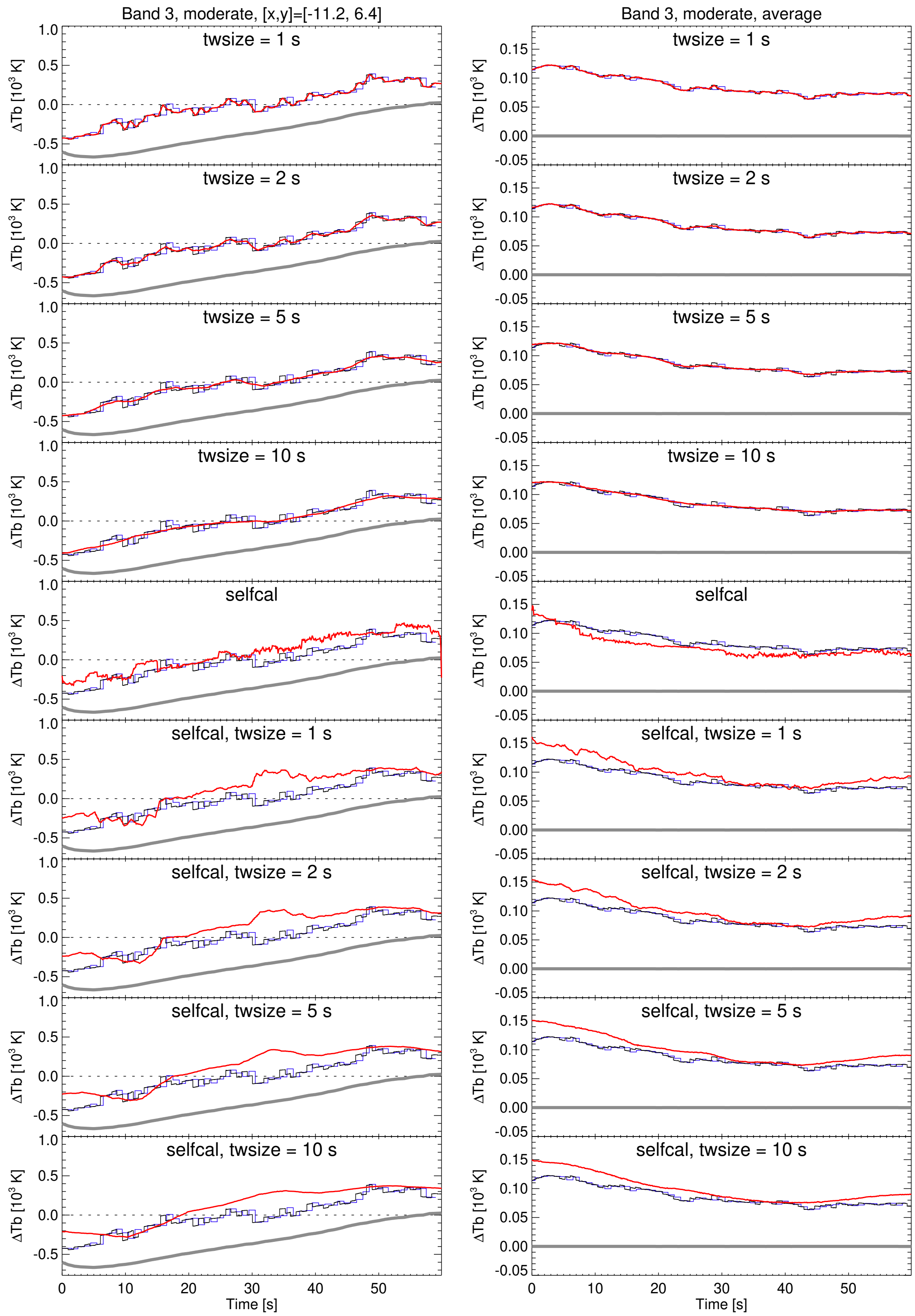

Figure 3.1: Brightness temperature as function time for Band 3 for the moderate weather scenario when exploiting the time domain to improve the data quality. Left: Selected pixel with coordinates given above the topmost panel. Right: Horizontal average (for all pixels within the mask). The rows show the results (red lines) for different choices of the twsize parameter in seconds with and without prior self-calibration. For comparison, the results without applying a running window (twsize=0, no self-cal.) for the sequences with $\Delta t = 0.1$ s (black) and $\Delta t = 1$ s (blue) and the convolved reference model (grey) are shown.

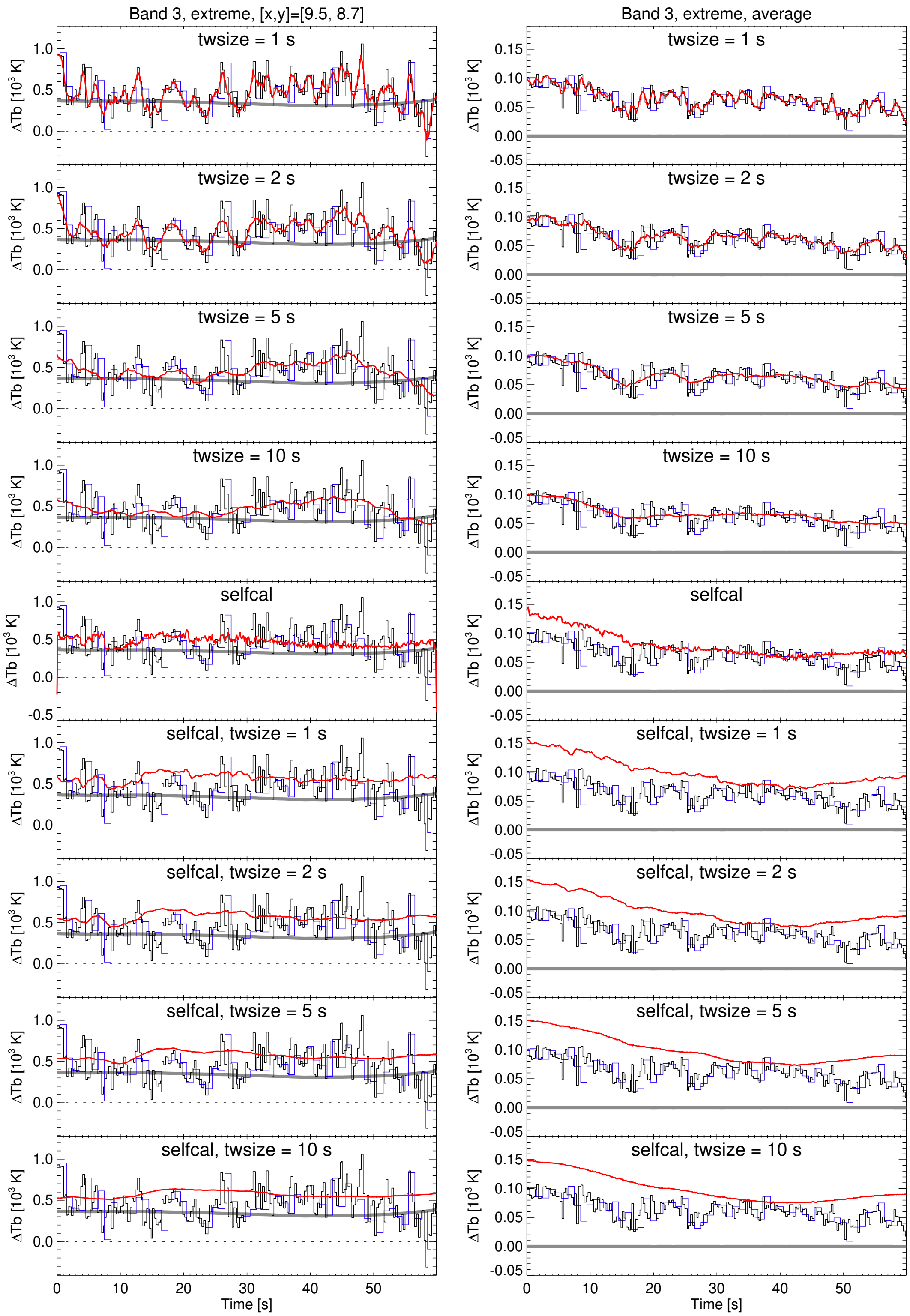

Figure 3.2: Brightness temperature as function time for Band 3 for the extreme weather scenario when exploiting the time domain to improve the data quality. Left: Selected pixel with coordinates given above the topmost panel. Right: Horizontal average (for all pixels within the mask). The rows show the results (red lines) for different choices of the twsize parameter in seconds with and without prior self-calibration. For comparison, the results without applying a running window (twsize=0, no self-cal.) for the sequences with $\Delta t = 0.1$ s (black) and $\Delta t = 1$ s (blue) and the convolved reference model (grey) are shown.

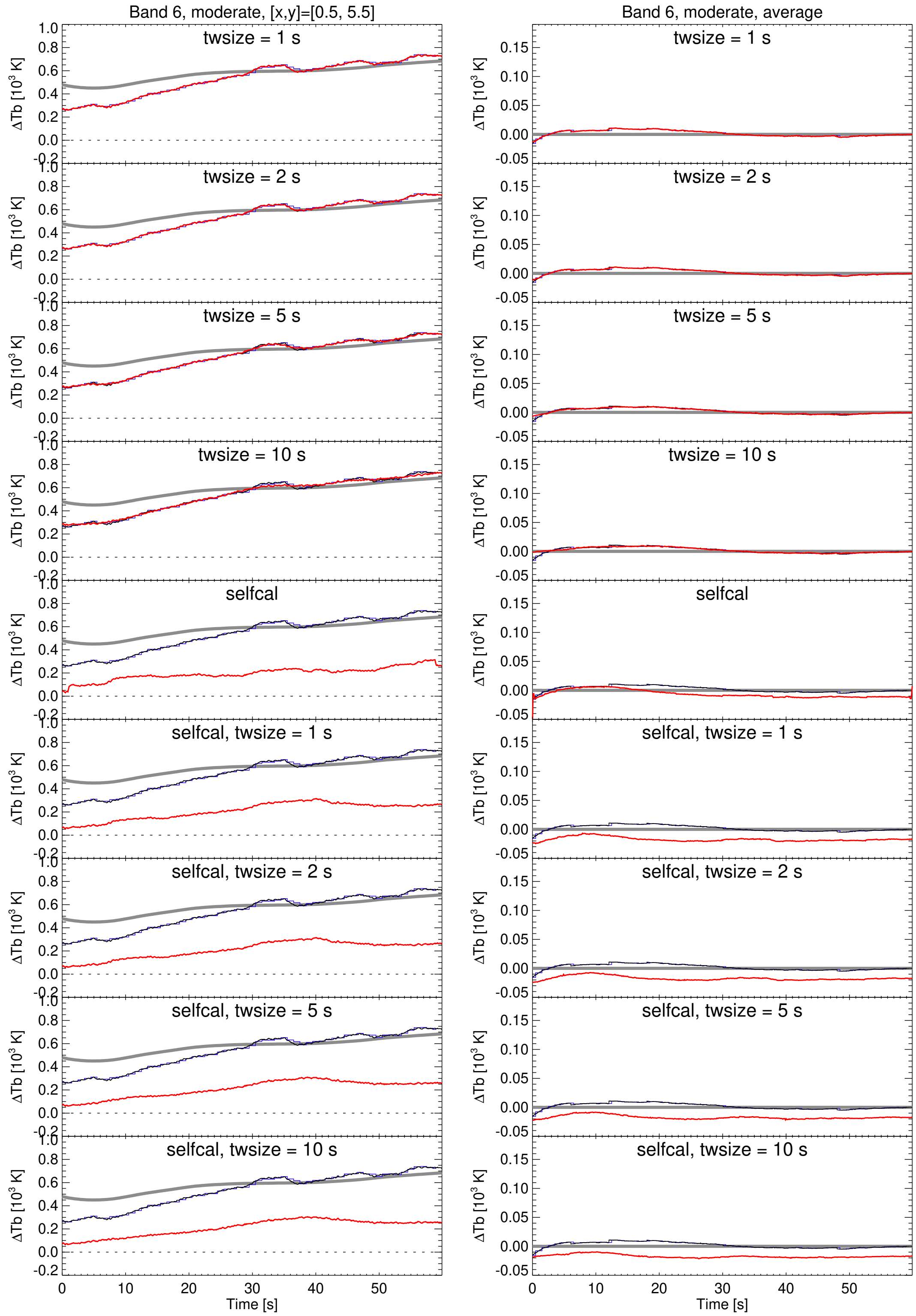

Figure 3.3: Brightness temperature as function time for Band 6 for the moderate weather scenario when exploiting the time domain to improve the data quality. Left: Selected pixel with coordinates given above the topmost panel. Right: Horizontal average (for all pixels within the mask). The rows show the results (red lines) for different choices of the twsize parameter in seconds with and without prior self-calibration. For comparison, the results without applying a running window (twsize=0, no self-cal.) for the sequences with $\Delta t = 0.1$ s (black) and $\Delta t = 1$ s (blue) and the convolved reference model (grey) are shown.

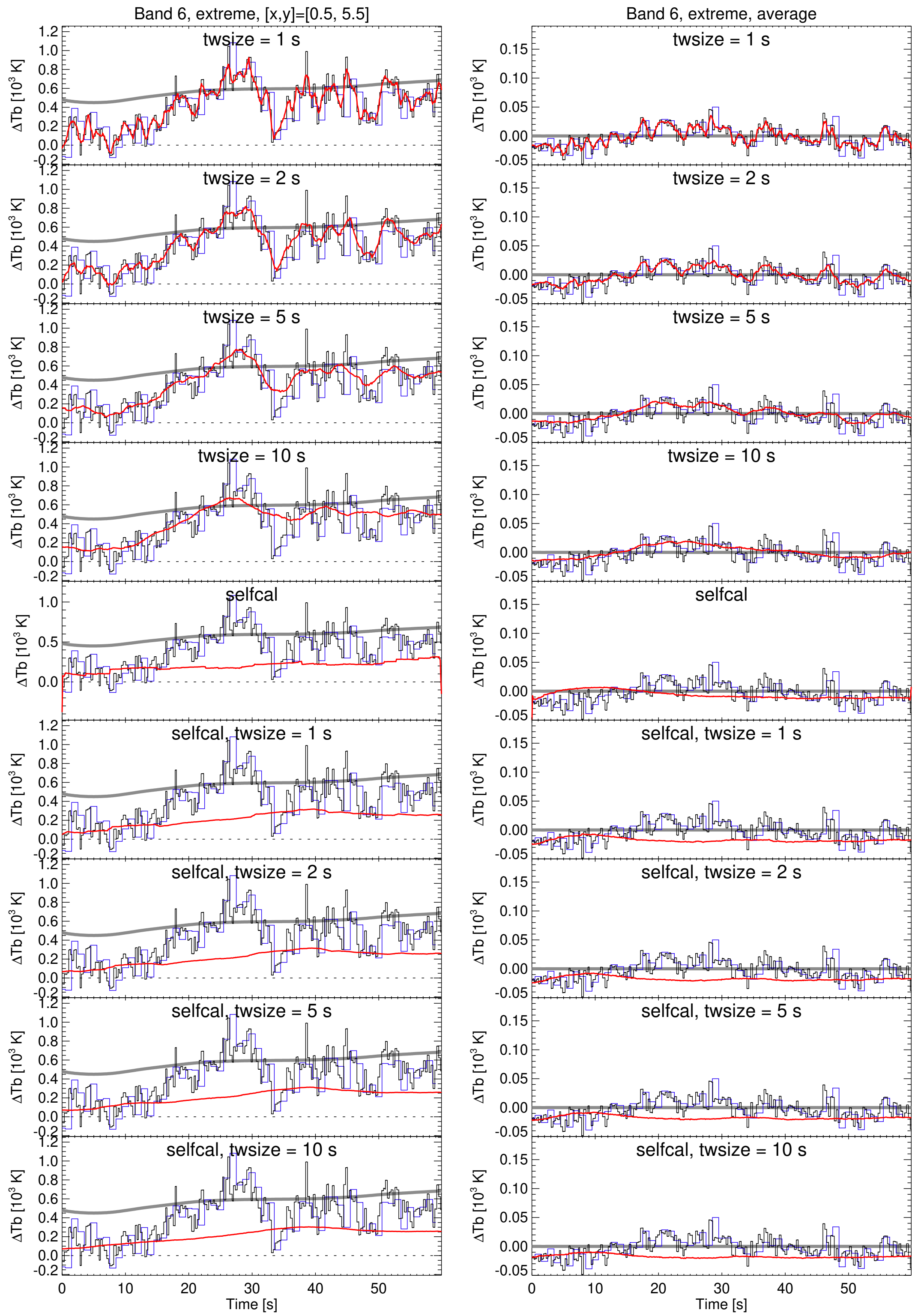

Figure 3.4: Brightness temperature as function time for Band 6 for the extreme weather scenario when exploiting the time domain to improve the data quality. Left: Selected pixel with coordinates given above the topmost panel. Right: Horizontal average (for all pixels within the mask). The rows show the results (red lines) for different choices of the twsize parameter in seconds with and without prior self-calibration. For comparison, the results without applying a running window (twsize=0, no self-cal.) for the sequences with $\Delta t = 0.1$ s (black) and $\Delta t = 1$ s (blue) and the convolved reference model (grey) are shown.

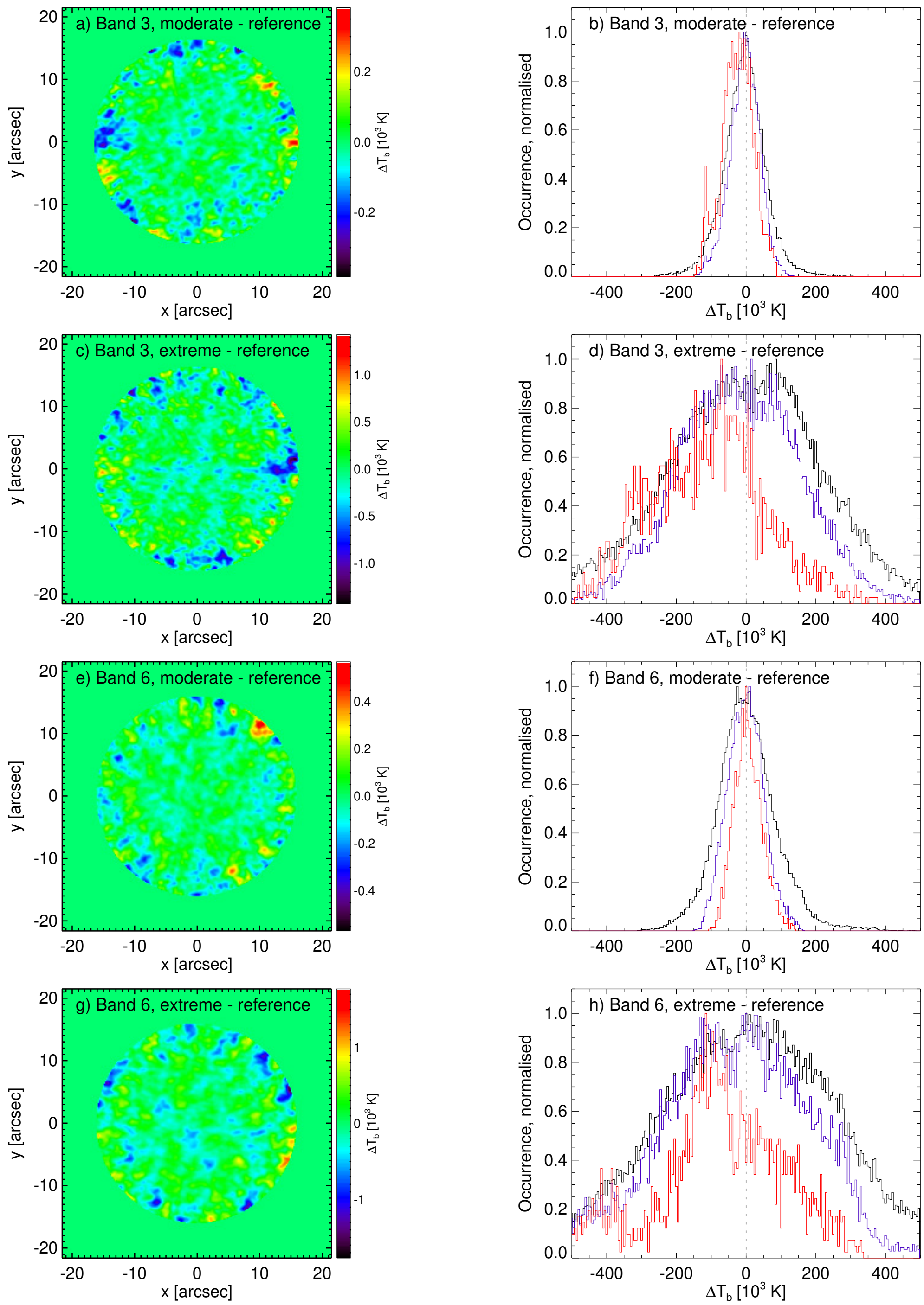

Figure 3.5: Brightness temperature differences for the first time step in the 0.1 s cadence series as produced with the basic imaging mode of SOAP (no sliding time windows, no self-calibration). Each row shows the difference map (left) and the corresponding histograms (right) for the selected bands (3 and 6) and the two selected scenarios (moderate and extreme). Each difference map was derived by subtracting the corresponding reference map (see Fig. 2.3c-d). Please note that the data range and the corresponding colour scales differ for each shown map. The histograms are calculated for the whole (circular) FOV (black), up to 50 % of the FOV radius (blue) and for 20 % of the radius (red).

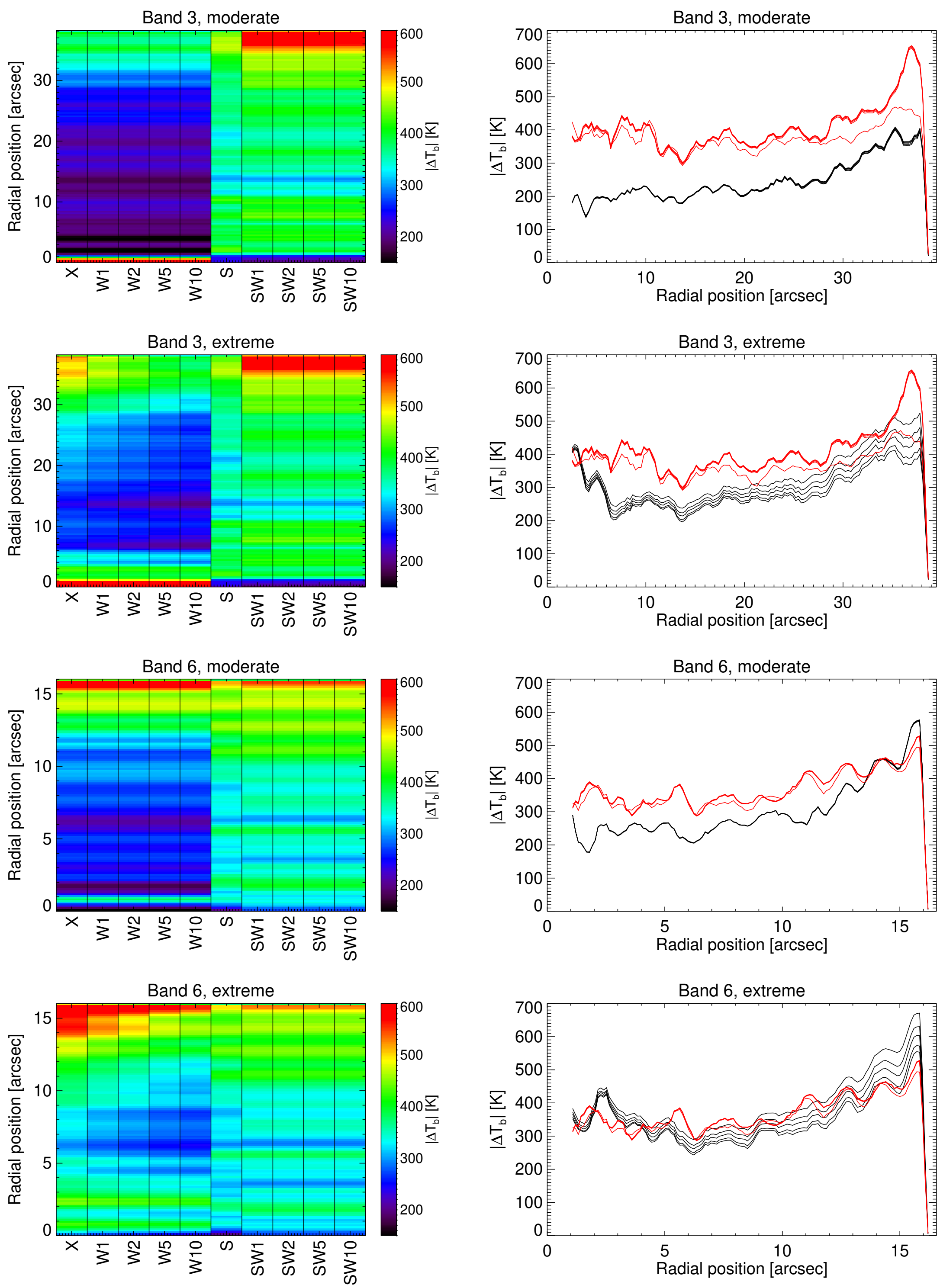

Figure 3.6: Absolute brightness temperature differences with respect to the reference model(s) for all considered imaging cases. Each row shows the different runs for Band 3 and 6 for the moderate and extreme scenario. In the right column, the radially and temporally averaged brightness temperature differences for the imaging runs without and with self-calibration are shown as black and red curves, respectively. As the curves are close to each other, the same data is shown as color-coded profiles in the left column with colours ranging from black ($\Delta T_b = 150\,\mathrm{K}$) to red ($\Delta T_b = 600\,\mathrm{K}$).

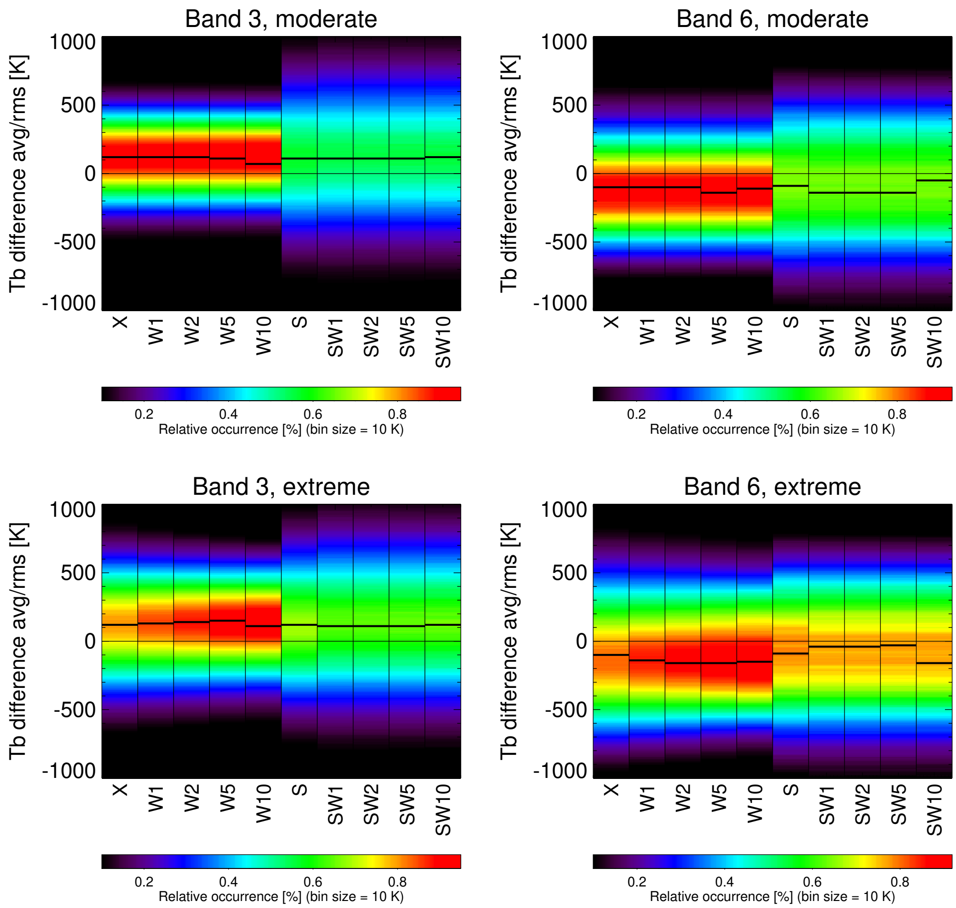

Figure 3.7: Histograms for the brightness temperature difference of the individual imaging runs for Band 3 (left column) and Band 6 (right column) and the moderate (top) and extreme scenario (bottom) with respect to the corresponding reference model. Only pixels with a distance of up to 70 % of the FOV radius are considered. The first five columns in each panel show the data for different widths of the sliding time window. A window size of 0 means that this technique is not applied and that those brightness temperature maps are calculated with SOAP frame by frame. The other five columns after equivalent but for the data with prior self-calibration (red). The histograms are scaled individually but presented on a common color scale for each panel. The data with prior self-calibration exhibit wider distributions and correspondingly lower values for the maximum relative occurrence of any Tb difference bin (notable as an apparent absence of red shades.)

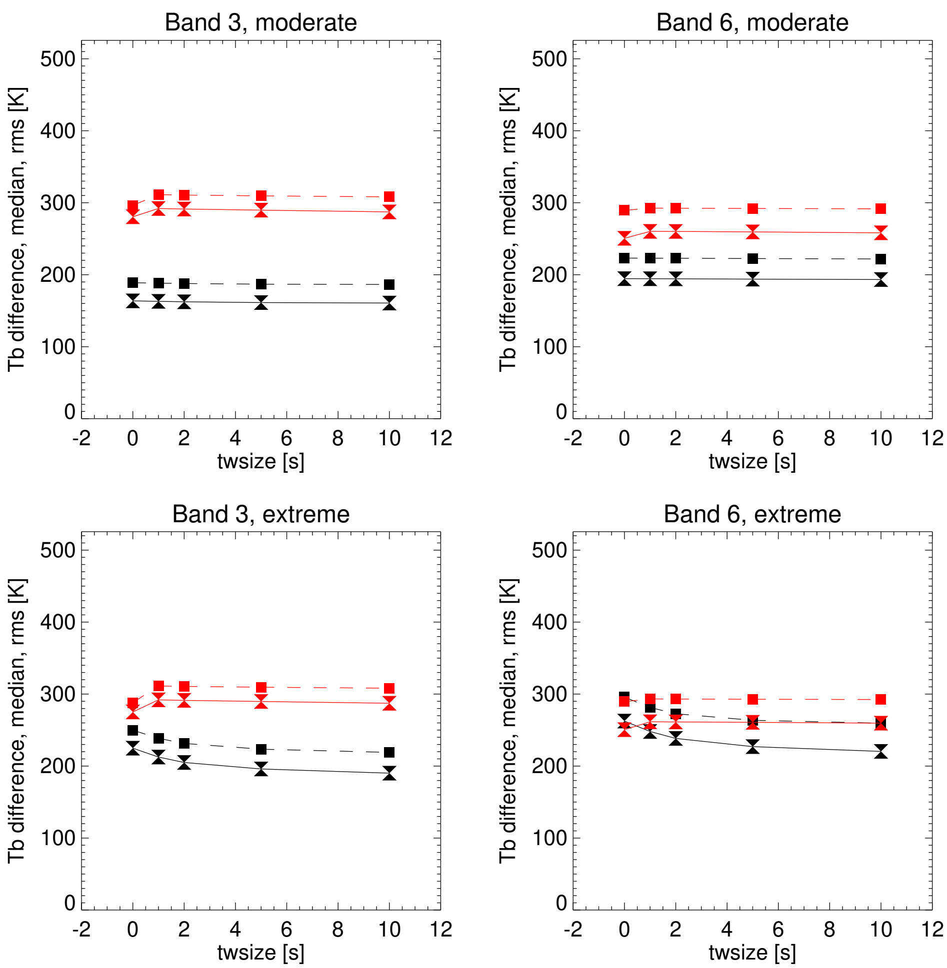

Figure 3.8: Data quality of the individual imaging runs for Band 3 (left column) and Band 6 (right column) and the moderate (top) and extreme scenario (bottom) without prior self-calibration (black) and with prior self-calibration (red). In each panel the average absolute brightness temperature with respect to the reference model (TDM, squares and dashed lines) and the its variation (TDV, double triangles and solid lines) are plotted as function of the size of the sliding time window. A window size of 0 means that this technique is not applied and that those brightness temperature maps are calculated with SOAP frame by frame (basic imaging).

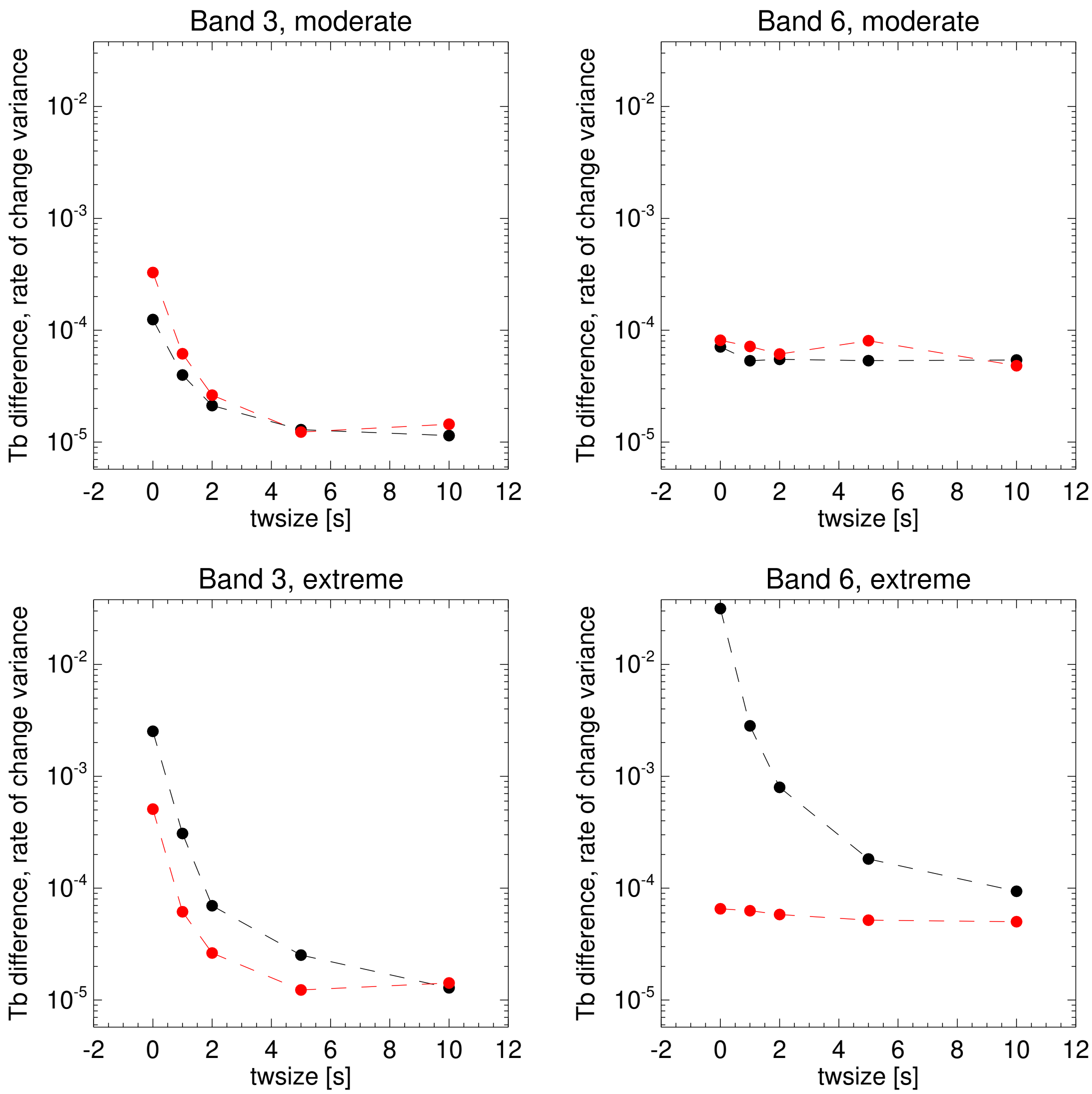

Figure 3.9: Variance of rate of change (VRoC) for the individual imaging runs for Band 3 (left column) and Band 6 (right column) and the moderate (top) and extreme scenario (bottom) without prior self-calibration (black) and with prior self-calibration (red). A window size of 0 means that this technique is not applied and that those brightness temperature maps are calculated with SoAP frame by fram (basic imaging).

4. Concluding remarks

This study demonstrates that imaging of solar ALMA data is challenging due to the sparse *uv*-sampling in the required snapshot imaging approach but that exploiting the time domain can increase the overall quality of the resulting time series of brightness temperature maps. Introducing a sliding time window in the imaging process, as implemented in SoAP, effectively reduces the noise already for short window sizes[1]. Under extreme conditions, observations at sub-second cadence can give an extra advantage and might allow for producing scientifically useful data from measurement sets that otherwise would be challenging to process. As the approach resembles an implicit time-averaging, the choice of the optimal window length and the resulting data quality certainly depend on the exact priorities of the intended scientific application. While the approach is advantageous for most solar studies, only adequately short time windows should be chosen for science cases focusing at changes at extremely short time scales ($\lesssim 1$ s).

It must be emphasised that interferometric aperture synthesis observations of a highly dynamic and complex source like the Sun with a limited number of baselines can by nature never achieve a perfect reconstruction of the source image. The results of this study therefore reveal differences and variations in the reconstructed brightness temperature maps that remain for otherwise optimised imaging strategies. Based on the scenarios considered in this study, remaining brightness temperature errors on the order of 200 K must be considered.

As alternative to sliding time windows, applying self-calibration substantially suppresses fluctuations and thus produces much more reliable results, confirming the impression gained from processing real ALMA data with self-calibration. This study reveals, however, that notable deviations from the true source images, as represented by the reference models used here, remain and can even be larger than compared to the results of basic imaging. However, apart from the systematic offsets, the temporal evolution of the reconstructed brightness temperatures is well reproduced when using self-calibration. It should also be noted that the scans used in this study have only a duration of 60 s while real data has scan durations of 600 s, which may make a difference for self-calibration. The

[1]Please note that these conclusions are based on the phase corruption according to the ***settrop()*** function. We recommend to review these conclusions once a more reliable phase corruption approach for solar observing conditions becomes available (see, e.g., Sects. 2.10-11 in the *Tech. Doc.* (Wedemeyer et al. 2023)).

offsets might be due to the fact that the reference model is too idealised [2] and can never be matched by data obtained with an interferometric array with a finite number of baselines. We recommend therefore to review in a future study if more suitable reference models can be constructed and/or if an algorithm can be devised that corrects for the brightness temperature offsets that might likely be due to the nature of observing a complex source like the Sun with an interferometric array. In conclusion, it is fair to say that the self-calibration technique and its current implementation for processing solar data have not yet been explored systematically so that the further development in this direction might lead to imaging with smaller remaining deviations from the true source.

Combining self-calibration with a sliding time window brings no substantial improvement in the cases considered in this study. This effect can be explained by self-calibration and sliding time windows being alternative ways of exploiting time domain information for noise reduction and their limitations for a highly dynamic source like the Sun.

As described in 2.2.1 in the *Imaging Report* (Wedemeyer et al. 2023), the model of the Sun used for this study is representative for a large part of the Sun as it includes an enhanced network structure with stronger magnetic fields and overarching coronal loops embedded in a Quiet Sun region. Consequently, the results and recommendations in this report apply to the majority of solar observations of typical targets (mostly Quiet Sun) that produce high-cadence time series. Other types of observations like observations of sunspots, at the solar limb, mosaics and single-dish mapping are not covered and would require a separate investigation.

Based on the cases studied here, it is recommended to further develop and test the techniques explored here. Moreover, although beyond the scope of this study, the inclusion of the Total-Power array in a full array combination imaging strategy might potentially help to overcome the missing short baselines, which might be particular important for high-cadence imaging of the Sun with notoriously sparse *uv*-sampling. It must also be noted that the imaging process, in particular the implementation of the CLEAN algorithm in itself is likely not ideal for solar data. It is therefore strongly recommended to evaluate and develop potentially more suitable methods, e.g. based on the Maximum Entropy Method (MEM).

[2] The reference model corresponds to a single-dish telescope with the same angular resolution as the synthetised beam of the simulated array but with perfect *uv*-coverage and no atmospheric or instrumental degradation. Please refer to Sect. 2.6 in the *Tech. Doc.* (Wedemeyer et al. 2023)).

Bibliography

Bastian, T. S., Bárta, M., Brajša, R., et al. 2018, The Messenger, 171, 25

De La Cruz Rodríguez, J., Szydlarski, M., & Wedemeyer, S. 2021, ART: Advanced (and fast!) Radiative Transfer code for Solar Physics., Zenodo

Gudiksen, B. V., Carlsson, M., Hansteen, V. H., et al. 2011, A&A, 531, A154+

Labeyrie, A. 1970, A&A, 6, 85

Puschmann, K. G. & Beck, C. 2011, A&A, 533, A21

Shimojo, M., Bastian, T. S., Hales, A. S., et al. 2017, Sol. Phys., 292, #87

van Noort, M., Rouppe van der Voort, L., & Löfdahl, M. G. 2005, Sol. Phys., 228, 191

Wedemeyer, S., Bastian, T., Brajša, R., et al. 2016, Space Sci. Rev., 200, 1

Wedemeyer, S., Fleishman, G., de la Cruz Rodríguez, J., et al. 2022, Frontiers in Astronomy and Space Sciences, 9, 967878

White, S. M., Iwai, K., Phillips, N. M., et al. 2017, Sol. Phys., 292, #88

Wöger, F., von der Lühe, O., & Reardon, K. 2008, A&A, 488, 375

Please also refer to the following two reports that are results of this study:

[Tech. Doc.]
Wedemeyer, S., Szydlarski, M., Carozzi, T., Toribio, M. C. et al. 2023, ESO "Advanced Study for Upgrades of the Atacama Large Millimeter/submillimeter Array (ALMA)" (CFP/ESO/16/11115/OSZ), *High-cadence Imaging of the Sun*, final study report review data package - DS4:
Technical documentation of the developed software packages

[Imaging Report]
Wedemeyer, S., Szydlarski, M., Carozzi, T., Toribio, M. C. et al. 2023, ESO "Advanced Study for Upgrades of the Atacama Large Millimeter/submillimeter Array (ALMA)" (CFP/ESO/16/11115/OSZ), *High-cadence Imaging of the Sun*, final study report review data package - DS4:
Recommendations for optimal post-processing of solar ALMA data